*Journal of Applied Electrochemistry* **30**: 247–257, 2000.



# Durability and thermal cycling of Ni/YSZ cermet anodes for solid oxide fuel cells

S. PRIMDAHL and M. MOGENSEN
*Risø National Laboratory, Materials Research Department, 4000 Roskilde, Denmark*

Received 26 March 1999; accepted in revised form 25 August 1999

*Key words:* cermet, durability, nickel, solid oxide fuel cell, thermal cycling, yttria stabilized zirconia

**Abstract**

The long-term properties of Ni/yttria stabilized zirconia (YSZ) cermet anodes for solid oxide fuel cells were evaluated experimentally. A total of 13 anodes of three types based on two commercial NiO powders were examined. The durability was evaluated at temperatures of 850 °C, 1000 °C and 1050 °C over 1300 to 2000 h at an anodic d.c. load of 300 mA $cm^{-2}$ in hydrogen with 1 to 3% water. The anode-related polarization resistance, $R_P$, was measured by impedance spectroscopy and found to be in the range of 0.05 to 0.7 $\Omega$ $cm^2$. After an initial stabilization period of up to 300 h, $R_P$ varied linearly with time within the experimental uncertainty. At 1050 °C no degradation was observed. At 1000 °C a degradation rate of 10 m$\Omega$ $cm^2$ per 1000 h was found. The degradation rate was possibly higher at 850 °C. A single anode was exposed to nine thermal cycles from 1000 to below 100 °C at 100 °C $h^{-1}$. An increase in $R_P$ of about 30 m$\Omega$ $cm^2$ was observed over the first two cycles. For the following thermal cycles $R_P$ was stable within the experimental uncertainty.

## 1. Introduction

Solid oxide fuel cell (SOFC) technology is at present approaching the economic requirements set by analysis of the consumer market, and two essential aspects are in focus: cost of production [1, 2] and demonstration of durability. The commercial requirements for SOFC systems include a cell and stack life in the order of 40–50 000 h [3]. Considering this life expectancy it is obvious that only very small degradation rates can be accepted for a commercial product.

All resistive limitations in an SOFC may suffer from degradation over time. Demonstration of total stack durability is of primary interest, but an analysis of the contribution to degradation made by each component is desirable. In the present work the anode polarization resistance, $R_P$, is investigated by impedance spectroscopy in a three-electrode setup. A thick electrolyte pellet is applied to minimize frequency-dependent errors [4].

It is well established that a key to better anode performance is optimization of the cermet structure. By increasing the active three-phase boundary (TPB) line where the three percolating phases Ni, yttria-stabilized zirconia (YSZ) and pores meet, better performance is achieved [5, 6]. The durability of the anodes can be expected, in part, to depend on the constancy of this TPB length. One of the important factors in structural stability is the mobility of Ni [7, 8].

The electrochemically active thickness of a cermet has been demonstrated to be about 10 $\mu$m at 1000 °C [9, 10]. The conductivity of the porous YSZ framework in the anode structure is believed to cause this limitation in the active anode thickness. Therefore, the conductivity degradation of YSZ electrolytes might contribute to cermet anode degradation [6, 11].

Long-term durability of cells and stacks has been demonstrated by several groups [12–14]. Studies of electrode conductivity over time have also been reported [15, 16]. A stable $R_P$ of 0.27 $\Omega$ $cm^2$ at 300 mA $cm^{-2}$ at 1000 °C has been demonstrated over 5500 h [17]. A degradation rate of about 47 m$\Omega$ $cm^2$ per 1000 h has been observed for Ni/YSZ cermet anodes on cells at 1008 °C and 300 mA $cm^{-2}$ [18].

Cooling cycles must be foreseen in stack life due to, for example, failure of other system components. The major concern in this respect is thermal expansion and contraction. The mechanical integrity of the anode/electrolyte interface is affected by the relative match of thermal expansion coefficients (TEC), which is again structure dependent in porous composites. A gradual increase in anode impedance of a factor of 2 has been demonstrated over 12 thermal cycles from 1000 °C to room temperature [19].

It is the aim of this study to demonstrate the durability and thermal cycle behaviour of Ni/YSZ cermet anodes as produced at Risø.

## 2. Experimental details

### 2.1. *Anode preparation*

Three-electrode electrolyte pellets, Figures 1 and 2, were produced by pressing, machining and sintering TZ8Y

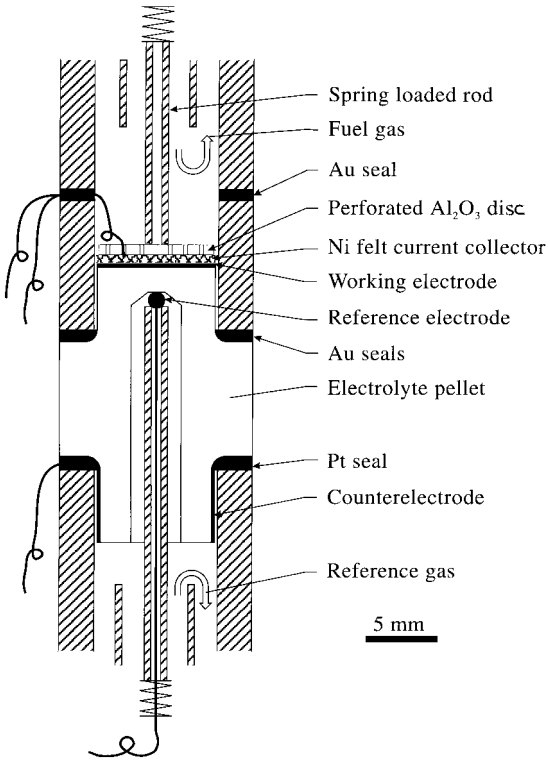


*Fig. 1.* One set-up used for characterizing anodes. The three-electrode electrolyte pellet (white body) is placed in a 2 atm set-up where the working electrode (anode) is in the fuel gas and the reference electrode and counterelectrode are in air.

($ZrO_2$ with 8 m/o $Y_2O_3$, Tosoh Corp.) at 1350 °C for 8 h.

A 40 to 50 $\mu$m thick anode (Type 'Matthey') was prepared by spraypainting. The ethanol based slurry was composed of green NiO (Johnson Matthey, 99% NiO) and TZ8Y, dispersed by polyvinyl pyrrilidone [20]. After deagglomeration in a ball mill, the YSZ particle size was about 0.4 $\mu$m. The combined particle size distribution of the prepared slurry was bimodal with fractions of approximately 0.4 $\mu$m and 10 $\mu$m in the volume ratio 9:1. The slurry was sprayed onto YSZ three-electrode pellets in layers of 10 to 20 $\mu$m and sintered for 2 h at 1300 °C after each layer. The Ni/YSZ volume ratio was 40/60 in the reduced cermet.

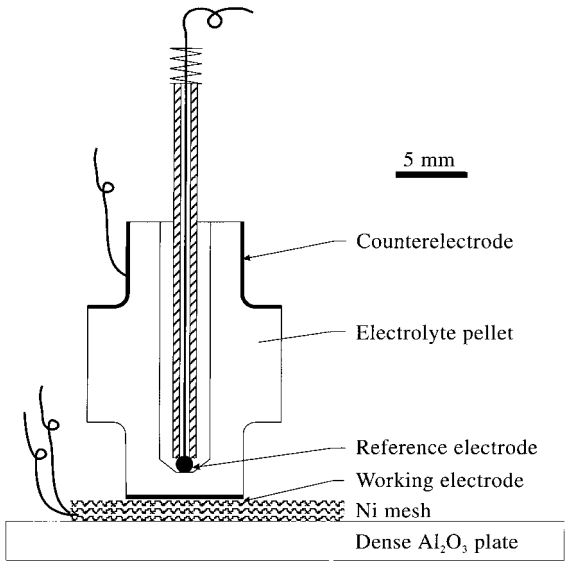


*Fig. 2.* Another set-up for characterizing anodes. The three-electrode pellet is placed in a 1 atm set-up with all electrodes in the fuel gas.

A number of anodes (type 'Matthey graded') were prepared and sintered as given above for the first 10 $\mu$m layer. A 25 $\mu$m thick layer containing NiO and TZ8Y in the weight ratio 64/36 was deposited. A second 25 $\mu$m thick layer was deposited, containing NiO and TZ8Y in the weight ratio 70/30 and subsequently sintered at 1300 °C for 2 h.

A third type of anode (type 'Baker') was produced similarly to the 'Matthey' anodes, except for the use of another NiO powder (J. T. Baker BV). The particle size distribution of the slurry was narrow with an average particle size of 0.35$\mu$m.

### 2.2. *Test set-up*

The YSZ three-electrode pellets were provided with a Pt-paste counter electrode and a Pt-ball reference electrode in the central bore.

A number of three-electrode pellets were tested in a two-atmospheres setup, Figure 1. This setup provided a reference atmosphere and a sealed cylindrical anode compartment. The fuel gas was fed through a concentric tube in the anode chamber. The reference electrode was placed in air, and a Nernst potential was measured. The working electrode of ~0.4 $cm^2$ area was contacted by a Ni-mesh (0.13 mm Ni wires with 0.50 mm wire spacing, Alfa/Johnson Matthey GmbH) pressed down by a 2 mm pushrod and a perforated $Al_2O_3$ disc of 2 mm thickness and 0.45 $cm^2$ area. The height from the anode surface to the feed tube was approximately 1 cm.

A one-atmosphere setup holding four three-electrode pellets at a time was used to increase the number of tested samples. The working electrode was contacted by three layers of Ni-mesh, supported by a dense $Al_2O_3$ plate of several $cm^2$, see Figure 2. A Nernst potential was measured against Pt/air by an immersed MgO-stabilized $ZrO_2$ sensor tube placed 15 mm from the samples. The temperature was measured at a distance of 5 mm from an anode, and additionally in contact with the $ZrO_2$ sensor tube.

### 2.3. *Electrochemical characterization*

The electrolyte geometry has been verified by finite element analysis to have a frequency stable, homogeneous current distribution, causing from 4% down to 2% error on an $R_P$ in the range 0.02–2 $\Omega$ $cm^2$ [4].

Impedance spectroscopy was conducted with an applied amplitude of 20 mV. The frequency range was 500 kHz to 0.01 Hz, or in some cases 50 kHz to 0.01 Hz.

The impedance was measured by a Solartron 1250 FRA combined with a Solartron 1286 ECI, a Solartron

1260 FRA with a Solartron 1287 ECI or a Solartron 1250 FRA combined with an EG&G 273 potentiostat. The three systems were verified on an appropriate test circuit to reproduce measurements within 1% of each other.

The $p_{O_2}$ was determined by the Nernst expression from open circuit voltage (OCV) vs Pt/air. The partial pressure of water $p_{H_2O}$ was determined from $p_{O_2}$ and $p_{H_2}$ by the following equation [21], valid for 1000 K $< T <$ 1300 K:

$$p_{H_2O} = 10^{-(2.958-13022/T)} \times p_{H_2}\sqrt{p_{O_2}} \quad (1)$$

The durability test of anodes was initiated by heating to operation temperature in 9% hydrogen in nitrogen saturated with water at 25 °C, then changing to a measurement atmosphere of hydrogen with either 1% or 3% of water. This atmosphere was maintained throughout the experiment with a total flowrate of 100 ml $min^{-1}$ (at 25 °C) dry gas.

For safety, an automatic system substituted the $H_2$ supply with 9% $H_2$ in nitrogen when any potentially dangerous situation occurred. The time but not the duration of such interruptions was recorded.

An anodic d.c. load of 300 mA $cm^{-2}$ was applied galvanostatic, and only briefly interrupted to reconnect and perform impedance measurements. A summary of tested anodes and conditions is given in Table 1.

A thermal cycle test was conducted as follows:

A Matthey anode was heated in 9% hydrogen with 3% water as described above, and allowed to stabilize for one week in hydrogen with 3% water. Thereafter, impedance spectroscopy at OCV was performed. Thermal cycling was conducted by cooling from 1000 °C to 95 °C over 10 h in 40 steps of no more than 25 °C. Reheating was at a rate of 100 °C $h^{-1}$. Below 600 °C and until 1000 °C was reestablished, a fuel gas with 9% hydrogen in nitrogen was used for safety reasons. A stabilizing period of one hour was allowed before impedance spectroscopy at OCV was performed. After nine thermal cycles the test was terminated.

All anodes were cooled in 9% hydrogen with 1% or 3% water. The in-plane resistance of the anode structures was qualitatively examined by measuring the d.c. resistance between two 0.3 mm Pt wire-ends at a distance of 0.4 and 0.7 mm. Selected cells were mounted in epoxy, cut and polished for structural characterization by low-vacuum SEM.

### 2.4. *Interpretation of impedance data*

Obtained impedance spectra were interpreted by equivalent circuits. Data were fitted by a nonlinear least-squares fitting routine, EQUIVCRT [22] using the following elements: $R$, $L$, $C$ and $Q$, representing resistance, inductance, capacitance and a constant phase element with an admittance $Y^* = Y_0(j\omega)^n$, respectively. Here $Y_0$ is an admittance factor, j the imaginary unit, $\omega$ the angular frequency and $n$ is the frequency power.

Phase errors at high frequency in the potentiostat as well as inductance in the leads was handled as an inductance $L$, of the system. A series resistance $R_S$ accounts primarily for the electrolyte resistance. Subcircuits of the type ($RC$) or ($RQ$) in a series arrangement were applied to describe arcs in Nyquist plots of impedance spectra.

Gas conversion and gas diffusion depending on the set-up geometry are known to contribute to electrochemical measurements, in these specific set-ups. Appropriate subcircuits and expected resistive values are given in the following. The notation I–III for arcs of increasing time constant applied elsewhere [23] is used.

An arc III at a summit frequency $f_S = 0.1$–10 Hz can be expected due to gas conversion in the fuel gas of a two-atmosphere setup [24]. An $(RC)_3$ subcircuit has been used, the expected resistance is about 0.2 Ω $cm^2$.

An arc II at a summit frequency $f_S = 10$–100 Hz can be expected due to diffusion limitation in a stagnant gas layer above the anode structure [25]. An $(RQ)_2$ subcircuit where $n_2 = 0.75$ has been used in the two-atmospheres setup, and $n_2 = 0.9$–1.0 in the one atmosphere set-up. The expectable resistances are of the order of 0.03–0.15 Ω $cm^2$, depending on the set-up.

An arc I at a summit frequency $f_S$ = 1–10 kHz has been demonstrated to depend on the structure of the anode cermet [23, 26]. The real part of this arc is considered to be the anode resistance, $R_P$, and thus the topic of the present study. This semicircle has been described by an ($RQ$) subcircuit where $n_1 = 0.80$ for cermet anodes [23, 26], and up to 0.9 for point anodes and anodes with a coarse structure [9, 27]. In several cases this arc has been demonstrated to consist of two overlapping arcs [9, 28]. Where two arcs could be resolved, they were referred to as arc Ia and arc Ib by increasing time constant, and each fitted to an ($RQ$)

*Table 1.* Anodes tested in hydrogen with 3 or 1% of water

| Anode | Type | Test temperature /°C | Duration of test /h | $p_{O_2}$ /atm | d.c. while measuring impedance/mA $cm^{-2}$ |
|---|---|---|---|---|---|
| A729-732 | Baker | 851 ± 1 | 1800 | 5–7 × $10^{-22}$ | 300 |
| A733-736 | Matthey | 851 ± 2 | 1500 | 2–6 × $10^{-21}$ | 300 |
| A627-628 | Matthey | 1004 ± 1 | 1300 | 3–5 × $10^{-18}$ | 300 |
| A648-649 | Matthey Graded | 1004 ± 1 | 1300 | 3–5 × $10^{-18}$ | 300 |
| A582 | Matthey | 1050 ± 2 | 2000 | 1 × $10^{-16}$* to 4–5 × $10^{-17}$ | 300 |
| A581 | Matthey | 1000 ± 2 | 9 cycles duration | 5–6 × $10^{-18}$ | Measured at OCV |

* $p_{O_2}$ changes after 1080 h due to a leak being sealed

subcircuit. The polarization resistance, $R_P$, was then found as the sum of $R_{1a}$ and $R_{1b}$.

In the one atmosphere setup an artifact arc at a frequency of about 0.5 Hz can be expected [25]. An $(RQ)_A$ subcircuit was used ($n_A = 0.9$), and the resistive value is about 0.01 $\Omega$ cm$^2$ in hydrogen with 3% water.

Obtained impedance spectra are 'preprocessed' before fitting. Spectra obtained at 850 °C exhibit erratic inductive loops at low frequency, and are cut short of impedance points with positive imaginary part. This constitutes a 'worst case' $R_P$, as the nature and interpretation of the loop is not known. At high frequency all obtained spectra are cut short of data points at frequencies higher than the vertical tangent.

## 3. Results

### 3.1. *Impedance spectra*

Examples of obtained impedance spectra are given in Figures 3 to 7. To illustrate the development in shape over the test duration, several spectra are given after normalization to electrode area and correction for inductance $L$ and series resistance $R_S$, which were determined by curve fitting.

Baker anodes tested at 850 °C, Figure 3, exhibit one dominant arc I with an $f_S$ of a few kHz, and a distinct arc II at $f_S \approx 10$ Hz. After a few hundred hours the arcs are no longer readily separated. After 400 h, and up to 1700 h, two dominant arcs are seen with $f_S$ in the kHz range (Ia) and at about 50 Hz (Ib). An inductive tail is noted below 10 Hz, the real part size of the tail varies erratically from 10% to about 50% of $R_{1a} + R_{1b}$ and is different for the four anodes. The overall shift in shape of impedance spectra is the same for the four tested anodes, but does not occur simultaneously indicating no dependence on a singular test event. In some spectra obtained after more than 400 h, the arc II at about 10 Hz is vaguely recognized.

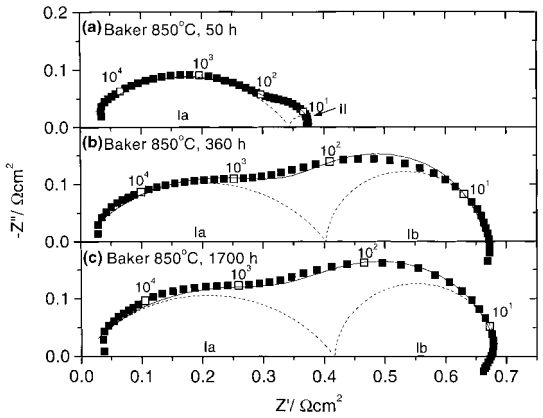


*Fig. 3.* Impedance spectra obtained on Baker anode A729 in the 1 atm set-up. At 850 °C in $H_2$ + 1% $H_2O$, 300 mA cm$^{-2}$. Area 0.42 cm$^2$. After (a) 50 h, $R_S$ = 2.7 $\Omega$ cm$^2$, $L = -8 \times 10^{-7}$ H, (b) 350 h, $R_S$ = 3.5 $\Omega$ cm$^2$, $L = -9 \times 10^{-7}$ H, and (c) after 1700 h, $R_S$ = 4.1 $\Omega$ cm$^2$, $L = -1 \times 10^{-6}$ H.

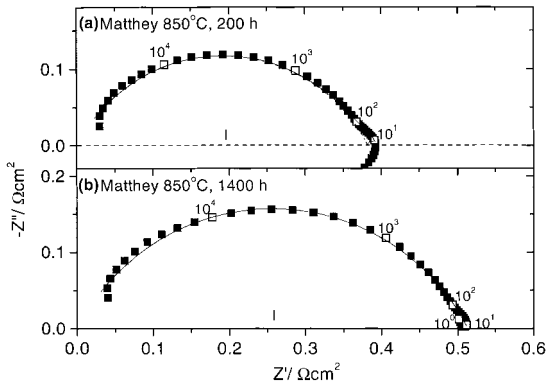


*Fig. 4.* Impedance spectra obtained on Matthey anode A733 in the 1 atm set-up. At 850 °C in $H_2$ + 3% $H_2O$, 300 mA cm$^{-2}$. Area 0.42 cm$^2$. After (a) 200 h, $R_S$ = 2.4 $\Omega$ cm$^2$, $L = -5 \times 10^{-7}$ H, and (b) after 1400 h, $R_S$ = 1.2 $\Omega$ cm$^2$, $L = -2 \times 10^{-7}$ H.

The possibility of the arc denoted Ib for Baker anodes being diffusion impedance outside the anode structure has been considered. A resistance of no more than 0.08 $\Omega$ cm$^2$ can be estimated at 1000 °C in 97% $H_2$ + 3% $H_2O$ [25]. Gas diffusion limitation is slightly deactivated by temperature, and inversely proportional to $p_{H_2O}$ at high $p_{H_2}$($R_D \sim T^2/p_{H_2O}$). Therefore, no more than 0.12 $\Omega$ cm$^2$ can be expected at 850 °C in 99% $H_2$ + 1% $H_2O$. Here the observed magnitude of arc Ib is from 0.10 to 0.30 $\Omega$ cm$^2$. It is thus considered unlikely that the arc denoted Ib is caused by diffusion impedance outside the electrode structure. This evaluation is supported by data on Matthey anodes in the same test configuration at 850 °C where no such arc Ib is observed, see below.

Matthey anodes at 850 °C, Figure 4, show one dominant arc I with $f_S$ in the kHz range, and a well-defined arc II with an $f_S$ of about 10 Hz. After a few hundred hours the low frequency arc II is transferred into a low frequency inductive tail for a period, thereafter arc II is again present.

Matthey anodes at 1000 °C, Figure 5, maintain two dominant arcs, one with $f_S$ in the kHz range (I) and one with $f_S$ below 100 Hz (II). This is a consistent feature of all impedance spectra, irrespective of the type of current collector structure (Matthey and Matthey graded). Very

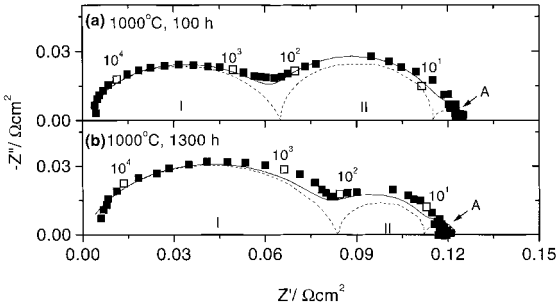


*Fig. 5.* Impedance spectra obtained on Matthey anode A628 in the 1 atm set-up. At 1000 °C in $H_2$ + 3% $H_2O$, 300 mA cm$^{-2}$. Area 0.42 cm$^2$. After (a) 100 h, $R_S$ = 0.9 $\Omega$ cm$^2$, $L = -3 \times 10^{-8}$ H, and (b) after 1300 h, $R_S$ = 1.3 $\Omega$ cm$^2$, $L = -6 \times 10^{-8}$ H.

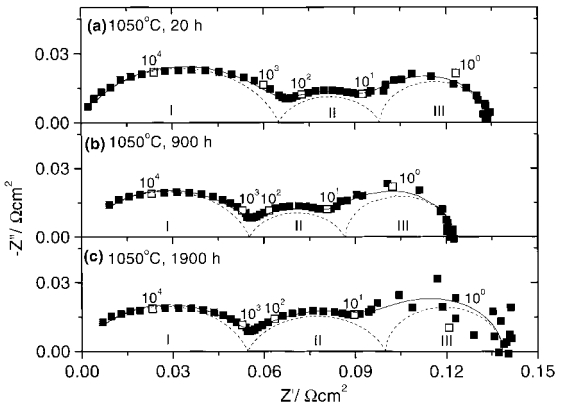


*Fig. 6.* Impedance spectra obtained on Matthey anode A582 in the 2 atm set-up. At 1050 °C in $H_2$ + 3% $H_2O$, 300 mA $cm^{-2}$. Area 0.40 $cm^2$. After (a) 20 h, $R_S$ = 0.7 Ω $cm^2$, $L = 1 \times 10^{-7}$ H, (b) 900 h, $R_S$ = 0.9 Ω $cm^2$, $L = 1 \times 10^{-7}$ H, and (c) after 1900 h, $R_S$ = 1.0 Ω $cm^2$, $L = 1 \times 10^{-7}$ H.

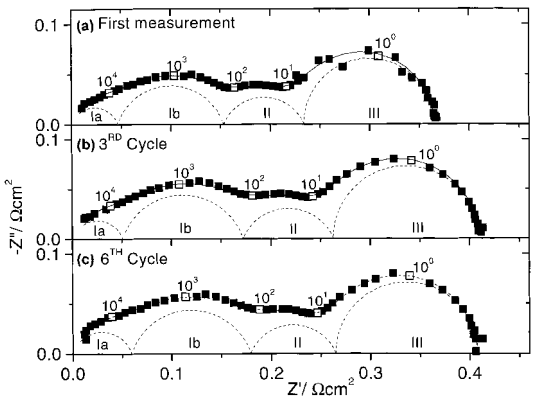


*Fig. 7.* Impedance spectra obtained on Matthey anode A581 in the 2 atm set-up. At 1000 °C in $H_2$ + 3% $H_2O$ at OCV. Area 0.40 $cm^2$. (a) First run, $R_S$ = 0.9 Ω $cm^2$, $L = -4 \times 10^{-8}$ H, (b) after 3 cycles, $R_S$ = 0.9 Ω $cm^2$, $L = -7 \times 10^{-8}$ H, and (c) after 6 cycles, $R_S$ = 0.9 Ω $cm^2$, $L = -2 \times 10^{-8}$ H.

little change is observed in the shape of the spectra over time.

The Matthey anode tested at 1050 °C exhibits three distinct arcs, Figure 6. Again an arc I with $f_S$ in the kHz range, a mid-frequency arc II with $f_S$ in the range 10–100 Hz and an arc III with $f_S$ at about 1 Hz is observed. Again the shape of spectra is fairly constant.

In the impedance spectra of the thermally cycled Matthey anode, Figure 7, four arcs are recognized. Two poorly resolved arcs Ia and Ib with $f_S$ in the kHz range, and again arc II with $f_S$ at about 10–100 Hz and arc III with $f_S$ at 1 Hz. The overall shape of the spectra is constant.

For each anode impedance data are fitted to the equivalent circuits given in Table 2. First, all the *n*-values are allowed to vary. Secondly, the *n*-values for arcs II, III and the artifact arc are fixed to the average values obtained from the first evaluation. In the third fit also arc I (or $I_a$ and $I_b$) are fixed at the average values obtained from the second evaluation. The final *n*-values are given in Table 2. The use of these fixed average *n*-values is based on a need for a systematic interpretation of the high-frequency end of impedance spectra, as will be elaborated in the discussion.

The real part values ($R_1$ or $R_{1a}$ + $R_{1b}$) obtained from durability tests are plotted against time after applying current in Figure 8 to Figure 11. The real part values ($R_{1a}$ and $R_{1b}$) obtained from the thermal cycle test are plotted against cycle number in Figure 12. The ordinate scale in each Figure is the double of the average $R_P$ value, to illustrate anode stability in a comparable form. Events during test that might have affected anode performance are marked. In general a small but systematic development in $R_P$ is observed. Scatter of the order of 10 to 25% is observed in $R_P$ for most tested

*Table 2.* Tested anodes, set-up geometry (Figures 1 and 2), selected equivalent circuit in the notation of [22], and *n*-values used in the final data fitting procedure for each anode

| Anode | Set-up | Equivalent circuit | $n_1(n_{1a}, n_{1b})$ | $n_2$ | $n_3$ | $n_A$ |
|---|---|---|---|---|---|---|
| A729 | 1 atm | $LR_S(RQ)_{1a}(RQ)_{1b}$ + $(RQ)_2$* | 0.60, 0.95 | 0.90* | – | – |
| A730 | | | 0.50, 0.95 | 0.90* | | |
| A731 | | | 0.75, 0.95 | 0.90* | | |
| A732 | | | 0.70, 0.95 | 0.90* | | |
| A733 | 1 atm | $LR_S(RQ)_1$ + $(RQ)_2$* | 0.70 | 0.90* | – | – |
| A734 | | | 0.65 | 0.90* | | |
| A735 | | | 0.75 | 0.90* | | |
| A736 | | | 0.70 | 0.90* | | |
| A627 | 1 atm | $LR_S(RQ)_1(RC)_2(RQ)_A$ | 0.80 | 1.00 | | 0.90 |
| A628 | | | 0.80 | 1.00 | | 0.90 |
| A648 | 1 atm | $LR_S(RQ)_1(RC)_2(RQ)_A$ | 0.75 | 1.00 | | 0.90 |
| A649 | | | 0.90 | 1.00 | | 0.90 |
| A582 | 2 atm | $LR_S(RQ)_1(RC)_2(RQ)_3$ | 0.80 | 0.75 | 1.00 | – |
| A581 | 2 atm | $LR_S(RQ)_{1a}(RQ)_{1b}(RQ)_2(RC)_3$ | 0.80, 0.80 | 0.75 | 1.00 | – |

*This subcircuit/value is only applied where the related arc is visually distinct

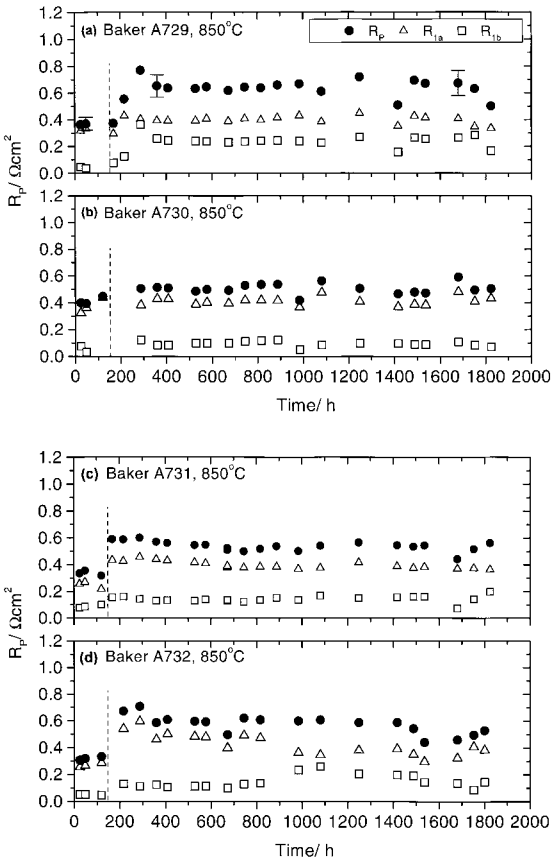


*Fig. 8.* $R_P$ for Baker anodes over time at 850 °C and 300 mA cm$^{-2}$ in hydrogen with 1% water. (a) A729, (b) A730, (c) A731 and (d) A732. $R_P = R_{1a} + R_{1b}$ as obtained by fitting obtained impedance spectra to the selected equivalent circuit given in Table 2. Dashed line indicates a temporary shift to 9% $H_2$.

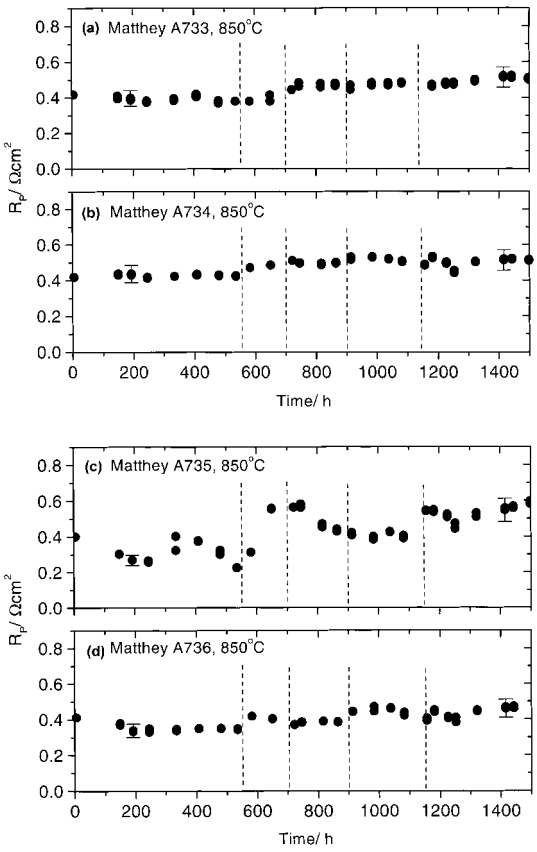


*Fig. 9.* $R_P$ for Matthey anodes over time at 850 °C and 300 mA cm$^{-2}$ in hydrogen with 3% water. (a) A733, (b) A734, (c) A735 and (d) A736. $R_P = R_1$ as obtained by fitting obtained impedance spectra to the selected equivalent circuit given in Table 2. Dashed lines indicate several temporary shifts to 9% $H_2$.

anodes. For Matthey anode A735 at 850 °C, Figure 9(C), the scatter is 50%.

Anodes were inspected after testing. The Matthey anodes appeared homogeneous when looking at the electrode surface, and the two-point in-plane resistance was about 1–1.5 Ω over 4–7 mm. The Baker anodes had a well-defined central region with a slightly darker colour covering about 1/3 of the working electrode area. The in-plane resistance was homogeneous over the working electrode surface and 50% lower than for Matthey anodes. Polished cross-sections of selected anodes and of reference anodes that were reduced for a short period (48 h) at 850 °C and 1000 °C were investigated using backscattered electrons in LV-SEM. The contrast between Ni and YSZ was insufficient for digital separation of the phases, but did allow for a visual identification in recorded images on screen. The Ni phase formed larger agglomerates encapsulating a number of YSZ particles, typical structures are given in Figure 13. This morphology was verified in optical microscopy. The Matthey anodes exhibit larger Ni-agglomerates, whereas Ni in the Baker anodes is better distributed among the YSZ particles. This is consistent with the particle size distributions measured prior to electrode deposition. Furthermore the porosity in the Baker anodes appears to be slightly lower than in the Matthey anodes. No development in structure of the tested anodes was observed compared with the reduced (<48 h) reference anodes. For Baker anodes, a change in the electrolyte contacting the anode in the central part of the working electrode is observed, Figure 14. The first 5 $\mu$m of the electrolyte under the electrode contains fine pores and in some regions a brighter (denser) substance is concentrated in cracks. This region of the electrolyte is well-defined against the underlying bulk electrolyte. No evidence of the Ni-mesh having collapsed to cause an increased diffusion limitation outside the anode structure was observed.

## 4. Discussion

### 4.1. *Error estimate*

In the following the scatter in obtained $R_P$ values is compared with an estimate of the experimental uncertainty.

Experimental conditions and limitations in the equipment influencing the determination of $R_P$ comprises gas

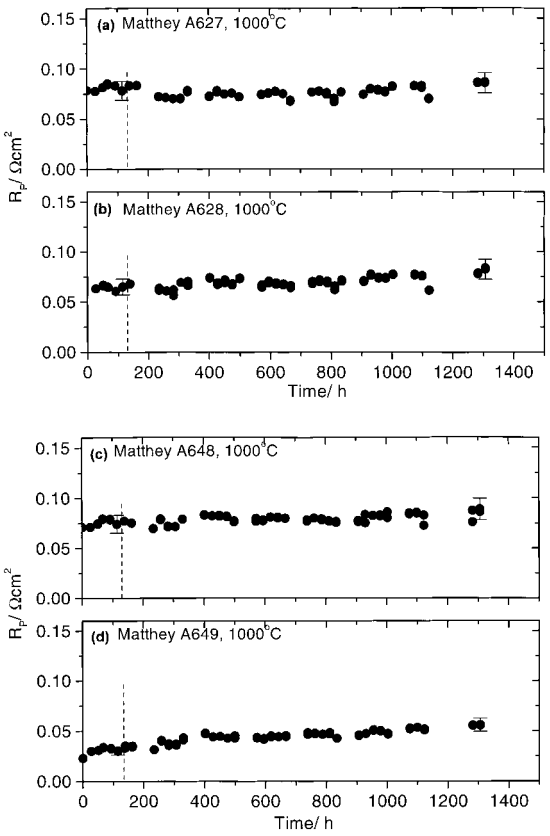


*Fig. 10.* $R_P$ for Matthey and Matthey graded anodes over time at 1000 °C and 300 mA cm$^{-2}$ in hydrogen with 3% water. (a) A627, (b) A628, (c) A648 (graded) and (d) A649 (graded). $R_P = R_1$ as obtained by fitting obtained impedance spectra to the selected equivalent circuit given in Table 2. Dashed line indicates a temporary shift to 9% $H_2$.

composition, temperature, level of quasi-equilibrium after interrupting the d.c. load, test cell geometry, instrument precision, quality of obtained impedance spectra and quality of the fit describing the spectra.

For these anodes the $R_P$ is known to be fairly insensitive to small changes in $p_{H_2}$ and $p_{H_2O}$ [23]. No systematic shift in $R_P$ is observed with the fluctuations in $p_{O_2}$, Table 1, or the $p_{O_2}$ shift in Figure 11. Temperature fluctuations of 2 °C (Table 1) can at the most cause a variation of 1.5% in $R_P$ considering an activation energy of 0.8 eV [23]. Consecutive measurements showed that

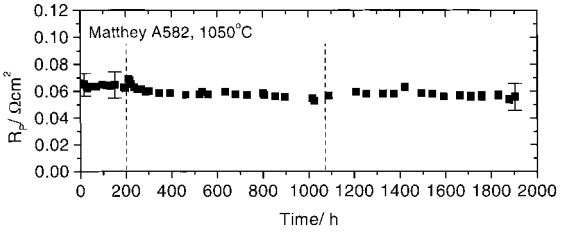


*Fig. 11.* $R_P$ for Matthey anode A582 over time at 1050 °C and 300 mA cm$^{-2}$ in hydrogen with 3% water. $R_P = R_1$ as obtained by fitting obtained impedance spectra to the selected equivalent circuit given in Table 2. First dashed line indicates a temporary (<0.5 h) shift to 750 °C, the second line indicates a permanent shift of $p_{O_2}$, see Table 1.

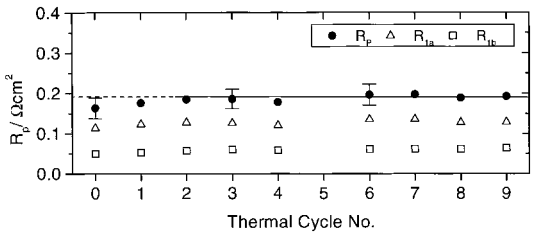


*Fig. 12.* $R_P$ by number of thermal cycles to 100 °C for Matthey anode A581 as measured at OCV at 1000 °C in hydrogen with 3% water. $R_P = R_{1a} + R_{1b}$ as obtained by fitting obtained impedance spectra to the selected equivalent circuit given in Table 2.

the variation in measured $R_P$ right after reconnecting cells to perform impedance measurements was less than 1%.

The error introduced by the position of the reference electrode in the test cell was taken to be 4% for $R_P$ values below 0.2 Ω cm$^2$ and 3% above [4].

The quality of obtained impedance spectra appears acceptable with respect to the signal/noise ratio, except at low frequencies above 850 °C. This part of the impedance spectra is dominated by known concentration polarization rather than $R_P$.

The instrument precision is set by the potentiostat rather than by the impedance analyzer, and amounts to about 3% and 3° above 10 kHz for the real part and imaginary part, respectively. The absolute real part error in $R_P$ is further increased by the rather high ratio of $R_S/R_P$ caused by the electrolyte geometry as discussed elsewhere [29]. However, for repetitive measurements on an electrochemical cell with a fairly constant response, only the apparatus drift is relevant. The uncertainty in the imaginary part of high frequency impedance points is drastically reduced by introduction of an unrestrained inductance $L$ in the equivalent circuit. Furthermore, fitting data to an equivalent circuit with fixed $n$-values allows a majority of data-points with limited phase errors to 'force' the shape of the high frequency part of the spectrum due to the unrestrained inductance. In conclusion a combined instrument precision of about 5% with respect to $R_P$ is estimated.

Based on the nonlinear-least-squares fit made to the experimental data, an error estimate was given by the fitting program for each parameter. The error in $R_P$ was taken to be the sum of errors on $R_{1a}$ and $R_{1b}$ divided by 2, as they were strongly correlated in the spectra. This error was determined for typical spectra, including those of Figures 3 to 7. For anodes tested at 850 °C the error was less than 1% for Matthey anodes, and 2–3% for Baker anodes. For Matthey anodes tested at 1000 °C the error was to 1–3%, at 1050 °C 1–5% and for the thermal cycle test an error of 2–4% was found.

As an estimate of the overall uncertainty, the above contributions are added to yield an error range 12–17%. These values are plotted as error-bars on the respective data-points in Figures 8 to 12. Because of the 50% scatter in data on the Matthey anode A735 in Figure 9(C), these data on are not considered in the following.

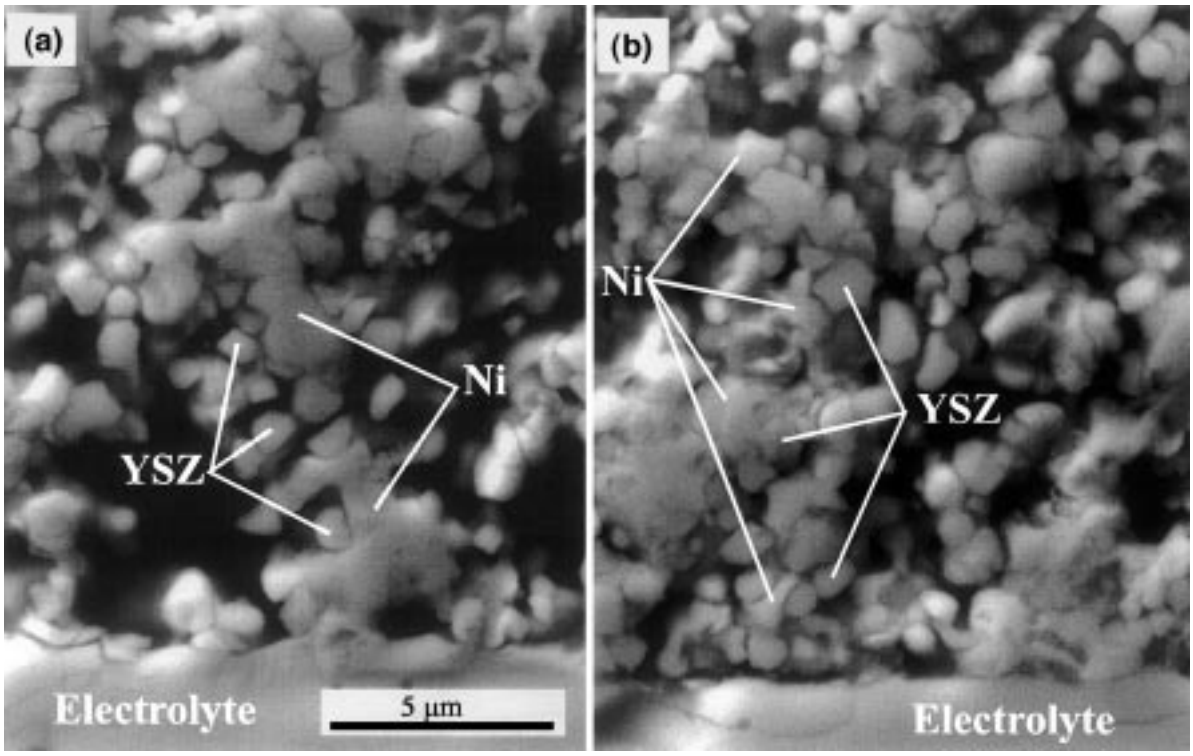


*Fig. 13.* SEM images of polished cross sections of anodes tested at 850 °C. (a) Matthey A736 and (b) Baker A729. Images taken 1–2 mm from the edge of the electrode.

### 4.2. *Degradation rates*

A fairly linear development in $R_P$ is observed over time in Figures 8 to 11. Test conditions ($p_{O_2}$, $T$) do not impact on $R_P$ beyond the uncertainty on data. For Baker anodes at 850 °C, Figure 8, the increase in $R_P$ is seen not to coincide with a temporary shift to 9% hydrogen.

A linear fit is applied to $R_P$ vs time. Data for the first 200 h on Baker anodes and for the first 300 h on the Matthey anode tested at 1050 °C are not included in the

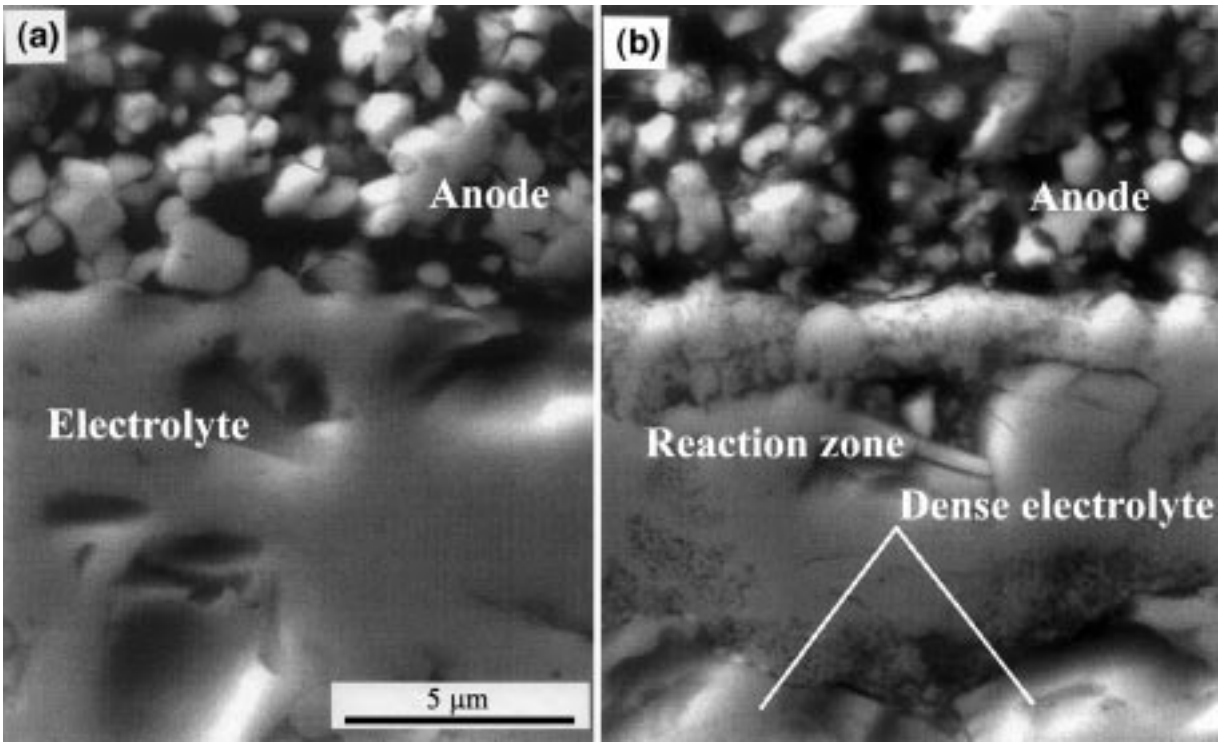


*Fig. 14.* SEM images of polished cross sections of Baker anode A729 showing the electrolyte in contact with the anode. (a) Undamaged electrolyte 1–2 mm from the edge of the electrode and (b) damaged electrolyte in the central part of the electrode.

fit. Slopes are compared with the linear fit value extrapolated to 0 h, $R_{P(0\,h)}$, as given in Table 3. The Matthey anode tested at 1050 °C indicate a slightly decreasing $R_P$ within the experimental uncertainty. Matthey anodes tested at 1000 °C indicate an increase of about 10 mΩ cm$^2$ per 1000 h. For the Matthey anodes tested at 850 °C the increase is about 100 mΩ cm$^2$ per 1000 h. However, these data are potentially affected by the four temporary shifts in the hydrogen partial pressure. Apparently the stability of Matthey anodes improves with increasing temperature.

No effect on durability is observed by applying a graded current collector on Matthey anodes. The Baker anodes exhibit decreasing $R_P$ with time at 850 °C. It should be noted that $R_P$ is considerably higher for Baker anodes than for Matthey anodes at this temperature.

Over the first two cycles of the thermal cycle test a degradation of 15 mΩ cm$^2$ per cycle or 9% per cycle is observed. This still falls within the uncertainty of the data. A linear fit to the datapoints for cycle 3 to cycle 9 of Figure 12 yields a constant performance within the experimental uncertainty.

### 4.3. *Degradation mechanisms*

The observed structural changes in the central part of the electrolyte under a Baker anode are presumably due to an unidentified solid state reaction. Under anodic load the atmosphere may contain substantial amounts of water in the central part of the electrode area increasing the $p_{O_2}$. The radial position of the electrolyte surface affected relates to limited gas exchange in the central electrode area caused by gas diffusion in the gap provided by the current collector [25]. Furthermore the porosity of the Baker anodes appear to be lower than of the Matthey anodes. Another issue in this context is purity of the technical NiO powders used. The effect of contaminants and additives on Ni/YSZ cermet anode performance and durability is not known.

Detrimental depletion of Ni at high $p_{H_2O}$ has been demonstrated for anode structures and related to a high partial pressure of volatile $Ni(OH)_2$ combined with the fuel gas sweeping the $Ni(OH)_2$ away [30]. At the conditions used here ($H_2/H_2O = 0.97/0.03$) a $Ni(OH)_2$ vapour pressure of less than $10^{-12}$ atm at 850 °C and about $10^{-9}$ atm at 1050 °C is predicted [30]. Therefore the impact of $Ni(OH)_2$ vapour transport is expected to be insignificant.

The conductivity of YSZ electrolyte exhibits a general degradation with time due to ordering of the oxide vacancies. This degradation amounts to about 30% at 1000 °C or 20% at 850 °C, without reaching a stable value over a period of 2000 h in air [31]. A comparable degradation of the bulk electrolyte conductivity can be observed in the $R_S$ values given in the captions of Figures 3 to 7. The fairly stable $R_P$ values measured in the present work indicate that ionic resistance in the electrolyte phase of the cermet is not contributing significantly to $R_P$.

Ni rearrangement by surface diffusion has an activation energy of about 1 eV, causing the diffusion coefficient to be a factor of 4.5 higher at 1050 °C than at 850 °C. It is considered unlikely that Ni surface diffusion causes the formation of a stable cermet structure in less that 100 h at 1050 °C, and a continuous change of structure over 1500 h at 850 °C.

### 4.4. *Recommendations*

There appears to be significant variation in the durability of nominally identical anodes tested simultaneously. It is recommended that better statistics are obtained by testing several identical samples, preferably in a multicell set-up.

*Table 3.* Performance and durability of tested anodes
Data are obtained at 300 mA cm$^{-2}$ and based on a linear fit over the indicated period of time. The change in polarization resistance, $\Delta R_P$, is given absolute and relative to the linearly extrapolated $R_P$ at 0 h, $R_{P(0\,h)}$

| Anode | Test temperature /°C | Time range considered /h | $R_{P(0\ h)}$ /mΩ cm$^2$ | $\Delta R_P$ /mΩ cm$^2$ per 1000 h | $\Delta R_P$ /% per 1000 h |
|---|---|---|---|---|---|
| A729 | 851 ± 1 | 200–1800 | 690 | −50 ± 30 | −7 ± 4% |
| A730 | | | 500 | 0 ± 20 | 0 ± 4% |
| A731 | | | 570 | −30 ± 10 | −5 ± 2% |
| A732 | | | 670 | −90 ± 20 | −13 ± 3% |
| A733 | 851 ± 2 | 0–1500 | 350 | +110 ± 10 | +31 ± 3% |
| A734 | | | 410 | +80 ± 10 | +20 ± 2% |
| A735* | | | – | – | – |
| A736 | | | 320 | +100 ± 10 | +31 ± 3% |
| A627 | 1004 ± 1 | 0–1300 | 75 | +3 ± 2 | +4 ± 3% |
| A628 | | | 62 | +11 ± 2 | +18 ± 3% |
| A648 | 1004 ± 1 | 0–1300 | 74 | +7 ± 1 | +9 ± 1% |
| A649 | | | 34 | +16 ± 1 | +47 ± 3% |
| A582 | 1050 ± 2 | 300–2000 | 59 | −1 ± 1 | −2 ± 2% |

* Not evaluated due to poor data quality

With the inherent uncertainty in measured $R_P$ of 12–17%, extrapolations in time are highly unreliable. Tests as performed in the present work are suggested to serve only as a qualification for starting durability tests of the order of 10 000 h.

The selected test geometries are not considered ideal, and for future tests the following approach is recommended. The low-frequency accuracy can be improved by avoiding concentration polarization (mass transport) outside the anode structure. In practice this is obtained by using an auxiliary electrode in face-to-face contact with the working electrode through a thin mesh, so that these electrodes experience the same current with opposite polarity [25]. Hereby the electrodes furnish reactants and removal of products for each other at a distance of the mesh thickness, provided the electrode reactions are reversible. This setup would also ensure a homogeneous gas access and current distribution for the working electrode. The conditions would then represent the expected conditions for an anode under a porous current collector rib or layer in a fuel cell stack. To establish representative conditions for the effect of $Ni(OH)_2$ vapour transport from 'uncovered' anodes between contact ribs of a stack interconnect, the gas flow conditions of the stack would have to be reproduced in the test setup.

To obtain better accuracy in the high-frequency impedance it is necessary to reduce the $R_S/R_P$ ratio. No practical method has been convincingly demonstrated which does not involve increased errors due to a frequency-dependent current distribution [4].

## 5. Conclusions

Anodes based on NiO from Johnson Matthey (Matthey anodes) were tested at temperatures from 850 to 1050 °C, and exhibited no significant degradation at 1050 °C. A degradation rate of 10 mΩ cm$^2$ per 1000 h was noted for anodes tested at 1000 °C, whereas anodes tested at 850 °C indicated even higher degradation rates.

A Matthey anode was tested over nine thermal cycles from 1000 °C to below 100 °C, and exhibited a degradation of about 15 mΩ cm$^2$ or 9% per cycle over the first two cycles, whereafter $R_P$ was constant within the experimental uncertainty.

Anodes based on NiO from Baker exhibited decreasing $R_P$ over time, but the values of $R_P$ were a factor of two higher than for the Matthey anodes. A reaction zone was detected in the underlying electrolyte in the central region of the working electrode where the gas access was limited. The possible reaction product and the cause of reaction were not established.

## Acknowledgement

This work was supported by the European Commission under contract JOE3-CT95-0005. Discussion with Dr N. Bonanos and Dr P.V. Hendriksen, Risø, was appreciated. The experimental data were generated as a result of the joint effort of members of the SOFC project group at Risø. Their contributions are gratefully acknowledged.

## References

1. M. Ippommatsu , H. Sasaki and S. Otoshi, *Int. J. Hydrogen Energy* **21** (1996) 129.
2. C. Bagger, N. Christiansen, P.V. Hendriksen, E.J. Jensen, S.S. Larsen and M. Mogensen, *in* F.W. Poulsen, N. Bonanos, S. Linderoth, M. Mogensen and B. Zachau-Chistiansen (Eds), 'High Temperature Electrochemistry: Ceramics and Metals', 17th Risø International Symposium on Materials Science (1996), p. 167.
3. S.P.S. Badwal and K. Foger, *Materials Forum* **21** (1997) 187.
4. J. Winkler, P.V. Hendriksen, N. Bonanos and M. Mogensen, *J. Electrochem. Soc.* **145** (1998) 1184.
5. J. Mizusaki, H. Tagawa, T. Saito, K. Kamitani, T. Yamamura, K. Hirano, S. Ehara, T. Takagi, T. Hikita, M. Ippommatsu, S. Nakagawa and K. Hashimoto, *J. Electrochem. Soc.* **141** (1994) 2129.
6. T. Norby, P.A. Osborg and H. Ræder, *in* U. Bossel (Ed.), Proceedings of the 'First European Solid Oxide Fuel Cell Forum', European SOFC Forum, Oberrohrdorf, CH, (1994), p. 671.
7. M. Mogensen and S. Skaarup, *Solid State Ionics* **86–88** (1996) 1151.
8. M.M. Murphy, J. Van herle, A.J. McEvoy and K.R. Thampi, *J. Electrochem. Soc.* **141** (1994) L94.
9. M. Brown, S. Primdahl and M. Mogensen, *J. Electrochem. Soc.*, submitted.
10. S. Sakamoto, H. Taria and H. Takagi, Denki Kagaku **64** (1996) 609.
11. S.P.S. Badwal, *Solid State Ionics* **52** (1992) 23.
12. S.C. Singhal, *in* U. Stimming, S.C. Singhal, H. Tagawa and W. Lehnert (Eds), '*Solid Oxide Fuel Cells*', **PV 97-40**, The Electrochemical Society Proceedings Series, Pennington, NJ (1997), p. 37
13. H.J. Beie, L. Blum, W. Drenckhahn, H. Greiner and H. Schisschl, *in* P. Stevens (Ed.), Proceedings of the 'Third European Solid Fuel Cell Forum', European SOFC Forum, Oberrohrdorf, CH (1998), p. 3.
14. W. Schäfer, H. Geier, G. Lindemann and D. Stolten, *in* F.W. Poulsen, J.J. Bentzen, T. Jacobsen, E. Skou and M.J.L. Østergård, (Eds.), 'High Temperature Electrochemical Behaviour of Fast Ion and Mixed Conductors', 14th Risø International Symposium on Materials Science, Roskilde DK (1993), p. 409.
15. P.H. Middleton, M.E. Seiersten and B.C.H. Steele, *in* S.C. Singhal, (Ed.), 'Solid Oxide Fuel Cells', **PV 89-11**, The Electrochemical Society Proceedings Series, Pennington, NJ (1989), p. 90.
16. L. Kinderman, F.W. Poulsen and C. Bagger, *in* P. Stevens, (Ed.), Proceedings of the 'Third European Solid Oxide Fuel Cell Forum', Poster section, European SOFC Forum, Oberrohrdorf, CH, (1998), p. 133.
17. T. Fukui, S. Ohara and K. Mukai, *Electrochem. Solid-State Lett.* **1** (1998) 120.
18. T. Iwata, *J. Electrochem. Soc.* **143** (1996), 1521.
19. A.C. Khandkar, S. Elangovan, M. Liu and M. Timper, *in* D.D. Macdonald and A.C. Khandkar, (Eds.), 'High Temperature Electrode Materials and Characterization', **PV 91-6**, The Electrochemical Society, Pennington, NJ (1991), p. 175.
20. C. Bagger, *in* '1992 Fuel Cell Seminar', Courtesy Associates, Inc. Washington, DC (1992), p. 241.
21. R. Hartung and H.-H. Möbius, *Chemie-Ing. Techn.* **40** (1968) 592.
22. B.A. Boukamp, *Solid State Ionics* **20** (1986) 31.
23. S. Primdahl and M. Mogensen, *J. Electrochem. Soc.* **144** (1997) 3409.
24. S. Primdahl and M. Mogensen, *J. Electrochem. Soc.* **145** (1998) 2431.

25. S. Primdahl and M. Mogensen, *J. Electrochem. Soc.* **146** (1999) 2827.
26. S. Primdahl and M. Mogensen, *in* [12], p. 530.
27. F.Z. Mohamedi-Boulenouar, J. Guindet and A. Hammou, *in* [12], p. 441.
28. S. Primdahl, B.F. Sørensen and M. Mogensen, *J. Am. Ceram. Soc.,* accepted.
29. M.J. Jørgensen, S. Primdahl and M. Mogensen, *Electrochim. Acta,* **44** (1999) 4195.
30. A. Gubner, H. Landes, J. Metzger, H. Seeg and R. Stübner, *in* [12], p. 844.
31. C.C. Appel, N. Bonanos, A. Horsewell and S. Linderoth, in preparation.